




Internal Electric Field Reconstruction and SAR Estimation of In-Body Antenna Using Inverse Equivalent Current Method

Rasyidah Hanan Mohd Baharin , *Student Member, IEEE*, Shuntaro Omi , *Member, IEEE*, Toru Uno , *Senior Member, IEEE*, and Takuji Arima, *Member, IEEE*

Abstract—In this article, we reconstruct the internal electric field due to a dipole antenna embedded in a dielectric phantom for developing a noninvasive specific absorption rate (SAR) measurement system. The reconstruction method is based on the surface equivalent theorem and boundary conditions, which relate the external field radiated from the embedded antenna to equivalent electromagnetic surface currents on the human body. The electric field data sampled at spatial points on a surface enclosing the phantom are used in the inverse calculation. All field integrals are discretized and numerically solved to obtain the electromagnetic currents on the phantom's surface. The internal electric field distribution and SAR value in a phantom can be calculated from the reconstructed surface currents if the electric properties of the phantom are known. The validity of the method was demonstrated numerically and experimentally using a dipole antenna embedded in the lossy rectangular phantom, which has a dielectric constant close to human skin tissue at 2.5 GHz. Comparison with forward numerical simulations has shown that the surface current and electric field distribution can be predicted with great precision. Carefully performing the experiments using a self-made phantom validated our numerical demonstration and provided satisfactory reconstruction results.

Index Terms—Antenna measurements, biomedical telemetry, electromagnetic fields, inverse problems, specific absorption rate (SAR).

I. INTRODUCTION

RECENTLY many kinds of wireless biomedical telemetry devices are deployed for disease prevention, diagnosis, monitoring, and even therapeutic functions. These devices are installed and operated at various locations. The wearable devices could be placed externally near the surface of the human body, contrary to implantable and ingestible devices that operate inside

the body [1], [2]. Even though internal devices, such as electrical pacemakers for the heart, or wireless capsule endoscopy (WCE) pills for monitoring the gastrointestinal tract are successful clinically, some concerns about the possible health effects of exposure to electromagnetic fields radiated from these devices are hard to be completely cleared up. Especially for a wireless device that communicates with equipment outside of the human body, a large power supply is required to compensate the internal propagation loss. Following that, the specific absorption rate (SAR) in W/kg was established as the safety standard [3]. Accordingly, the evaluation and measurement of SAR are indispensable for biomedical telemetry devices and electronic equipment that radiates electromagnetic (EM) waves.

The widely used SAR measurement method is performed by insertion of an electric field probe inside of a tank filled with a liquid phantom that is illuminated by the antenna under test (AUT) [4]. This method, although straightforward, poses a set of disadvantages. First, there is the issue of instability of liquid phantom. Second, while the volumetric three-dimensional (3-D) electric-probe scanning is typically accurate, the method is invasive in nature. The collection and postprocessing of such volumetric data will consume a considerably long time.

Hence, a noninvasive SAR measurement is necessary to address the inherent disadvantages of the conventional method.

In this context, this article's objective is to reconstruct the internal \mathbf{E} -field of the phantom using the 2-D-probe data, with the measurement taking place externally on an arbitrary surface outside of the phantom. As a result, the SAR value can easily be estimated from the predicted \mathbf{E} -field. This proposition allows the usage of a solid phantom that has a more stable shape and dielectric properties [5]. Furthermore, the surface data's computational load is expected to be less than that of the volumetric data because this method requires only 2-D data on the measurement surface enclosing the phantom.

Over the past decade, there were several pieces of literature that attempt to relate the electric and magnetic field (\mathbf{E} and \mathbf{H} , respectively) measurement with SAR of phantom through boundary element method (BEM) with each work highlighting a slightly different aspect. In [6]–[8], it is shown that the \mathbf{E} and \mathbf{H} on the phantom's surface can be related to its external fields through solving a linear equation derived from the discretized BEM integral equation that expresses field continuity condition. Here, AUT is not considered.

Manuscript received December 29, 2020; revised April 29, 2021; accepted June 3, 2021. Date of publication June 30, 2021; date of current version October 13, 2021. (Corresponding author: Rasyidah Hanan Mohd Baharin.)

Rasyidah Hanan Mohd Baharin is with the Department of Electronic and Information Engineering, Tokyo University of Agriculture and Technology, Tokyo 184-8588, Japan (e-mail: rh.baharin@gmail.com).

Shuntaro Omi is with the Applied Electromagnetic Research Institute, National Institute of Information and Communications Technology, Tokyo 184-0015, Japan (e-mail: shuntaro-omi@nict.go.jp).

Toru Uno and Takuji Arima are with the Tokyo University of Agriculture and Technology, Tokyo 184-8588, Japan (e-mail: uno@cc.tuat.ac.jp; t-arima@cc.tuat.ac.jp).

Color versions of one or more figures in this article are available at <https://doi.org/10.1109/TEMC.2021.3088522>.

Digital Object Identifier 10.1109/TEMC.2021.3088522

The scope of this article is then classified as inverse equivalent surface current method (ECM) or source reconstruction (SR). We refer this method as ECM-SR, henceforth. In [9], the field relations between AUT and phantom are established whereby the boundary integral equations are derived based on the surface equivalence principle. All of the integral equations are discretized and simultaneously solved using Poggio–Miller–Chan–Harrington–Wu–Tsai (PMCHWT) formulation. Then, EM fields inside of a phantom illuminated by an external AUT are reconstructed using the surface measurement data that encloses all target objects in [10]. In addition, probe correction is applied to practical measurement. More recently, a study in [11] studies a similar setup of SR but adds a separate link between currents so that the numerical inversion algorithm becomes more stable. Although these pieces of literature were useful for building up the fundamental understanding of this article, they have been already carried out with AUT located outside of the phantom. This article focuses on a new application where the AUT is placed inside of the phantom.

The purpose of this article is to establish a method for calculating the internal field of the phantom with an embedded AUT using the ECM-SR approach for noninvasive SAR estimation. The SR is performed using a modified version of the method in [10] in which its difference will be explained briefly. The field measurements are performed on the surface encapsulating both test subjects (phantom and AUT), after the full-probe correction for the receiver is applied to a quantitative measurement of \mathbf{E} -fields. The phantom used here is a cuboidal-shaped human tissue equivalent phantom. This setup emulates a simplified situation of a stationary implantable or ingestible antenna inside of a human body. It is shown in numerical simulations that the proposed method can precisely reconstruct both the surface currents and internal \mathbf{E} -field for the human equivalent phantom. In the case where the measured data are used, the current distribution on the surface of the cuboid phantom exhibits severe distortion with possible reasons explained. Nevertheless, the surface current magnitude and internal \mathbf{E} -field distribution were calculated satisfactorily.

In Section II, the ECM-SR procedure employed in this article is explained in detail. The theoretical formulations and methodology are also included. Section III presents the numerical results of the reconstructed currents, internal \mathbf{E} -field, and SAR estimation. Section IV shows the experimental results for validation. It briefly includes the preparation of the phantom and the experimental setup for precise measurements. Finally, Section V concludes this article.

II. SR PROCEDURE

A. Basic Formulations

The configuration of the dosimetry problem is shown in Fig. 1. The AUT is located inside of a closed surface S_A in the phantom of known permittivity and conductivity with the closed surface S_P . The field data are measured on sampling point \mathbf{R} on an arbitrary surface S_M , where $\mathbf{E}(\mathbf{R})$ is the electric field at the observation point \mathbf{R} , at which the probe is placed.

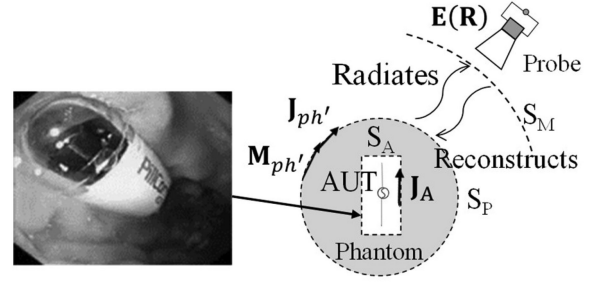


Fig. 1. Configuration of noninvasive SAR measurement for the in-body antenna. On the left-hand side is a photo of the endoscopy capsule PillCam that allows the visualization of the gastrointestinal system.

Within an inverse source framework, the aim is to use the external field measurement to deduce the internal field inside the phantom. By applying Huygen's principle (surface equivalence theorem) and appropriate boundary conditions, primary sources can be replaced by equivalent secondary sources. Thus, equivalent electric and magnetic currents $\mathbf{J}_{ph'}$ and $\mathbf{M}_{ph'}$ respectively, can be assumed on a closed surface S_P enclosing the phantom. Similarly, S_A is the surface of AUT and its current is corresponding to \mathbf{J}_A . It has been demonstrated in [9]–[11] that either electric or magnetic current is sufficient for representing the \mathbf{E} -field radiated from the primary source; hence, this article will consider only \mathbf{J}_A as the current source flowing on S_A . We refer this formulation as the \mathbf{J} -type single current equation formulation (\mathbf{J} -SEqF).

First, we will explain the radiation problem when AUT is located outside of the phantom. In an external AUT, the dosimetry considers that there are two kinds of radiation, first, direct ones from AUT, and second, indirect ones, which is caused by scattering and from the hidden area sandwiched between AUT and phantom [10]. The \mathbf{E} -field representation, in this case, is given as follows:

$$\mathbf{E}(\mathbf{R}) = -\eta_0 \mathcal{L}_{S_A}^{k_0}(\mathbf{J}_A, \mathbf{R}) - \eta_0 \mathcal{L}_{S_P}^{k_0}(\mathbf{J}_{ph}, \mathbf{R}) + \mathcal{M}_{S_P}^{k_0}(\mathbf{M}_{ph}, \mathbf{R}) \quad (1)$$

where the first term on the right-hand side (RHS) of (1) indicates direct propagation from AUT to the probe, while the second and third terms are due to external scattering. η_0 and k_0 are the wave impedance and wavenumber in a vacuum, respectively. \mathcal{L} and \mathcal{M} are the integral operators for the electric current and magnetic current, respectively, and defined as follows:

$$\mathcal{L}_S^{k_n}(\mathbf{X}, \mathbf{R}) = j k_n \iint_S \left[\frac{1}{k_n^2} \nabla G^{k_n}(\mathbf{R}, \mathbf{R}') \nabla' \cdot \mathbf{X}(\mathbf{R}') + G^{k_n}(\mathbf{R}, \mathbf{R}') \mathbf{X}(\mathbf{R}') \right] dS' \quad (2)$$

$$\mathcal{M}_S^{k_n}(\mathbf{X}, \mathbf{R}) = \iint_S \nabla G^{k_n}(\mathbf{R}, \mathbf{R}') \times \mathbf{X}(\mathbf{R}') dS' \quad (3)$$

where \mathbf{X} is the EM currents \mathbf{J} or \mathbf{M} , and $G^{k_n}(\mathbf{R}, \mathbf{R}')$ is the scalar Green's function. The superscript k_n on the integral operators indicates the wavenumber used in Green's function with its subscript $n = 0$ for free space, and $n = 1$ is for the phantom. When the AUT is inside of phantom, the modification

to (1) becomes (4) as follows:

$$\mathbf{E}(\mathbf{R}) = -\eta_0 \mathcal{L}_{S_P}^{k_0}(\mathbf{J}_{ph'}, \mathbf{R}) + \mathcal{M}_{S_P}^{k_0}(\mathbf{M}_{ph'}, \mathbf{R}) \quad (4)$$

$$\eta_0 \mathbf{H}(\mathbf{R}) = \frac{1}{jk_0} \nabla \times \mathbf{E}(\mathbf{R}) \quad (5)$$

where the equivalent EM currents on the AUT are now included with that of the phantom; the received data on the probe are the collection of radiation from one body. The first and second terms on the RHS in (4) refer to electric fields due to $\mathbf{J}_{ph'}$ and $\mathbf{M}_{ph'}$ on the phantom surface S_P . This is mostly similar to the meaning of terms as in (1), but the subscript of \mathbf{J} and \mathbf{M} on the RHS of (4) is instead written as ph' , the annotation ($'$) is to indicate that the EM currents on S_P are a result of internal scattering (reflection and refraction) of electric field and magnetic field of AUT, \mathbf{E}_A and \mathbf{H}_A , respectively, originating from inside of the phantom. The well-established equivalent EM currents and their relation to the electric and magnetic field is given as

$$\mathbf{J}(\mathbf{R}') = \hat{\mathbf{n}} \times \mathbf{H}(\mathbf{R}') \quad (6a)$$

$$\mathbf{M}(\mathbf{R}') = \mathbf{E}(\mathbf{R}') \times \hat{\mathbf{n}} \quad (6b)$$

where $\hat{\mathbf{n}}$ is the outward normal vector on S_P . Then, we can elaborate the matrices of EM currents and radiated field using the derivation of PMCHWT formulation [14]. In a bounded homogenous phantom, the unknown surface currents $\mathbf{J}_{ph'}$ and $\mathbf{M}_{ph'}$ can be related to \mathbf{E}_A and \mathbf{H}_A by the following expressions, (7) shown at the bottom of this page.

Compared with the inverse formulation in [10], (7) is the result of removing the matrix $[-\eta_0 \mathcal{L}_{S_P}^{k_0} \mathcal{M}_{S_P}^{k_0}]$, which is the scattering of AUT due to phantom in the free space environment and without the effect of k_1 . The equation is then further modified by omitting the magnetic current of AUT (J-SEqF). The matrix operator on the RHS acts on two vectors $\mathbf{J}_{ph'}$ and $\mathbf{M}_{ph'}$ in the following manner of the matrix equation, (8) shown at bottom of this page.

The inverse operator $(A)^{-1}$ on the RHS of (7) and (8) calculates the currents on the phantom's surface S_P with respect to incident EM fields radiated from AUT. Subscripts on the integrals indicate observation surfaces, S_P being phantom and S_A for AUT.

As for solving the surface current densities of \mathbf{J}_A , the Rao–Wilton–Glisson (RWG) was selected as the triangular basis function of method of moments (MoM) in a manner that the current distribution on S_A can be expanded as a weighted sum,

expressed as follows:

$$\mathbf{J}_A = \sum_{n=0}^N a_n f_n^{S_A}(r_A) \quad (9)$$

where a_n is the unknown expansion coefficient, $f_n^{S_A}$ is the RWG vector function with respect to S_A , and r_A is the point on each triangular meshes [13], [14]. The triangle discretization of $\mathbf{J}_{ph'}$ and $\mathbf{M}_{ph'}$ for the object scattering analysis is also done similarly as (9). Then, by solving (8), $\mathbf{J}_{ph'}$ and $\mathbf{M}_{ph'}$ can be obtained to solve (4). From here, we know that from the equivalent theorem, \mathbf{E} -field at any points inside a uniform and homogenous phantom can be calculated and it is given by (10). This is the final form of the information used to calculate SAR value.

$$\mathbf{E}(\mathbf{R})_{in} = \eta_1 \mathcal{L}_{S_P}^{k_1}(\mathbf{J}_{ph'}, \mathbf{R}) - \mathcal{M}_{S_P}^{k_1}(\mathbf{M}_{ph'}, \mathbf{R}). \quad (10)$$

Variable η_1 is the characteristic impedance inside the phantom. Accordingly, the integral operators in (2) and (3) also must be in terms of k_1 .

B. Probe-Correction Scheme on ECM-SR

Theoretically, electric fields observed at $\mathbf{E}(\mathbf{R})$ are influenced by factors, such as the measurement probe's direction dependence and its finite-size dimensions. Hence, the influence of the inverse operators and probe characteristics on the measured surface data must be governed by probe correction to attain correct reconstruction results. The measured signal at probe can be rewritten as a weighted volumetric integral of the probe's open-circuit voltage $U(\mathbf{R}_m)$, where \mathbf{R}_m is the individual point of probe sampling location. The integral weighted by a spatial vector weighing function $w_m(\mathbf{R})$ is given as (11) and expanded by (12)

$$U(\mathbf{R}_m) = \iiint_{V_{probe}} w_m(\mathbf{R}) \cdot \mathbf{E}(\mathbf{R}) dV' \quad (11)$$

$$U(\mathbf{R}_m) = \mathcal{W} \left(F_{S_P}^L(\mathbf{J}_{ph'}, \hat{\mathbf{k}}) + F_{S_P}^M(\mathbf{M}_{ph'}, \hat{\mathbf{k}}), \mathbf{R}_m \right) \quad (12)$$

where \mathcal{W} is the translating and weighing operator and $\hat{\mathbf{k}}$ is a unit vector in direction \mathbf{k} ; $\mathbf{k} \hat{\mathbf{k}} = \mathbf{k}$. The operators $F_{S_P}^L$ and $F_{S_P}^M$ correspond to the Fourier operations on the electric and magnetic current integrals on the surface of phantom, $\mathcal{L}_{S_P}^{k_0}$ and $\mathcal{M}_{S_P}^{k_0}$, respectively. The emphasis is deploying only a far-field pattern in an fast multipole method (FMM)—multilevel fast

$$\begin{bmatrix} \mathbf{J}_{ph'} \\ \mathbf{M}_{ph'} \end{bmatrix} = \left(\hat{\mathbf{n}} \times \begin{bmatrix} -\mathcal{L}_{S_P}^{k_0} - \mathcal{L}_{S_P}^{k_1} & \mathcal{M}_{S_P}^{k_0} + \mathcal{M}_{S_P}^{k_1} \\ \mathcal{M}_{S_P}^{k_0} + \mathcal{M}_{S_P}^{k_1} & \mathcal{L}_{S_P}^{k_0} + \mathcal{L}_{S_P}^{k_1} \end{bmatrix}^{-1} \right) \begin{bmatrix} \hat{\mathbf{n}} \times \mathbf{E}_A \\ \hat{\mathbf{n}} \times \eta_0 \mathbf{H}_A \end{bmatrix} \quad (7)$$

$$\begin{bmatrix} \mathbf{J}_{ph'} \\ \mathbf{M}_{ph'} \end{bmatrix} = \left(\hat{\mathbf{n}} \times \begin{bmatrix} -\mathcal{L}_{S_P}^{k_0} - \mathcal{L}_{S_P}^{k_1} & \mathcal{M}_{S_P}^{k_0} + \mathcal{M}_{S_P}^{k_1} \\ \mathcal{M}_{S_P}^{k_0} + \mathcal{M}_{S_P}^{k_1} & \mathcal{L}_{S_P}^{k_0} + \mathcal{L}_{S_P}^{k_1} \end{bmatrix}^{-1} \right) \begin{bmatrix} -\hat{\mathbf{n}} \times \eta_0 \mathcal{L}_{S_A}^{k_1} \\ \hat{\mathbf{n}} \times \mathcal{M}_{S_A}^{k_1} \end{bmatrix} [\mathbf{J}_A] \quad (8)$$

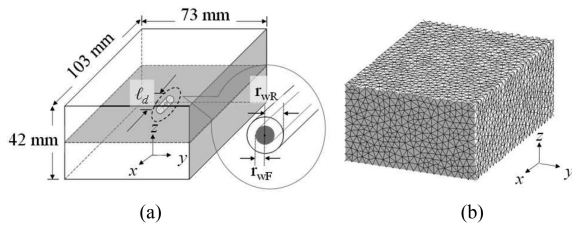


Fig. 2. Cuboid phantom. (a) Geometry dimension. (b) Surface mesh of 5732 triangles generated using GMSH, AUT cylinder inside is not visible.

multipole method representation as the centerpiece of full-probe correction in this ECM-SR scheme. We adapt this method in the same manner as the articles presented in [10] and [15]. Generally, the implementation of the probe-correction technique does not differ from the previous studies; however, the resultant equivalent currents used in (12) are due to the internal scattering of AUT propagating from inside of phantom, as mentioned in Section II-A.

There are many methods to implement (11) and (12) in a computationally efficient manner for the matrix inversion. We have implemented a generalized minimal residual solver and a least-square-based iterative method for the equation system, where only the evaluation of vector/matrix products is required for the solution.

The advantage of this technique is the independence of the measurement probe's distance, provided that the interaction between the probe and phantom is not extremely strong. For example, the probe can be placed either close to the target to acquire a maximum quantity of diagnostic information or from some distance in which the current distribution on the probe is smoother and less influenced by the nearby target or phantom. On the other hand, only the measurement from the spherical surface can be considered because the weighing function \mathcal{W} contains the plane-wave expansion that utilizes the spherical Hankel function of the second kind for the spherical near-field transformation. Appropriate transformation must be applied accordingly if the probe is scanning on a cylindrical or cartesian coordinate system.

Another point to note is that the system was constructed with the boundary integral formulations as its main foundation. Therefore, only a homogenous phantom of single permittivity and conductivity value could be used. One could consider the effective dielectric constants, ϵ_{eff} , such as used in the calculation of multilayer substrates for patch or microstrip antenna [16], [17], as a temporary solution to utilize ECM-SR in a heterogenous structure that is more close to the realistic human body, but it is not yet tested for this article.

III. NUMERICAL DEMONSTRATION

In this section, we implement the SR method, as explained in Section II. The numerical results are compared with ones computed by commercial simulator FEKO v2020.1.

A. Simulation Parameters

The geometry of the simulation is shown in Fig. 2(a). A dielectric phantom with dimensions 42 mm \times 103 mm \times 73 mm

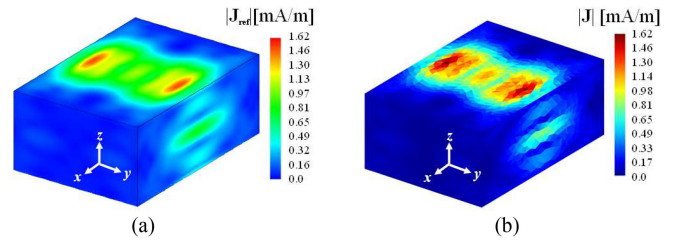


Fig. 3. Electric current distribution on S_P . (a) Generated by FEKO. (b) Reconstructed.

of a known permittivity $\epsilon_r = 48.7$ and $\sigma = 1.66$ (S/m) is embedded with a horizontal perfect electric conductor (PEC) dipole antenna in the center. It is operating at 2.5 GHz, which is the upper limit of one of the industrial, scientific, and medical radio frequency band [18], with AUT length $\ell_d = 4.3$ mm or a quarter wavelength in the phantom λ_{ph} . In this article, the dipole antenna as the AUT is considered as the simplest model of WCE. A commercial WCE ranges from 23 mm \times 11 mm to 31.5 mm \times 11.6 mm ($L \times D$) in dimension, depending on its medical purpose [19]. Thus, the corresponding AUTs installed in these devices will naturally be designed at a much smaller size and the selected ℓ_d is deemed practical for the investigated frequency.

The small free space gap of 0.01 mm was set between the AUT and dielectric in order to feed the dipole antenna properly as well as to avoid simulation error. The radius of a cylindrical wire in FEKO is given as $r_{wF} = 0.05$ mm and the reconstruction surface of GMSH is set slightly above it at $r_{wR} = 0.1$ mm to avoid numerical instability caused by MoM used in FEKO. Fig. 2(b) shows the cubic phantom in the meshing software GMSH [20] that has the same geometry as Fig. 2(a), with the reconstruction surface meshed into small triangle patches. The spherical sampling enclosure for \mathbf{E} -field data is 0.6 m distance (5λ) from the cuboid, elevation angle is $0 \leq \theta \leq \pi$ and $0 \leq \phi \leq 2\pi$, that is the full sphere scan was performed for collecting the data. The angular sampling interval was $\Delta\theta = \Delta\phi = 5^\circ$. In the numerical tests, spherical scanning near the field data was generated from FEKO and only the phi-component (ϕ) data were used for reconstruction. For SAR calculation, the mass density was set as $\rho = 1000$ kg/m³. Finally, for the least-square solver, the solver tolerance was set as 10^{-6} to ensure high accuracy of the reconstructed results.

B. Reconstruction Results

The reconstructed surface current using the ECM-SR implementation is shown in Fig. 3, while the equivalent internal electric field distribution observed in a cut of the yz -plane through the center is shown in Fig. 4. ‘‘Generated by FEKO’’ means the data are calculated by FEKO as a forward problem, while ‘‘reconstructed’’ is obtained by applying the method, as proposed in Section II. The results show good agreement between the FEKO and reconstructed results.

To see this more clearly, the internal \mathbf{E} -field distribution and resultant SARs along the z -axis at $x = y = 0$ are shown in Fig. 5 and Fig. 6, respectively. For these figures, the logarithmic scale was provided in addition to the linear scale for a clear vision of

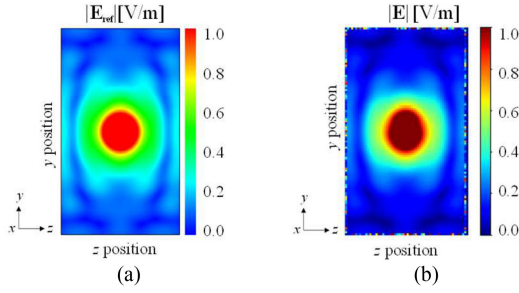


Fig. 4. Internal $|\mathbf{E}|$ distribution. (a) Generated by FEKO. (b) Reconstructed.

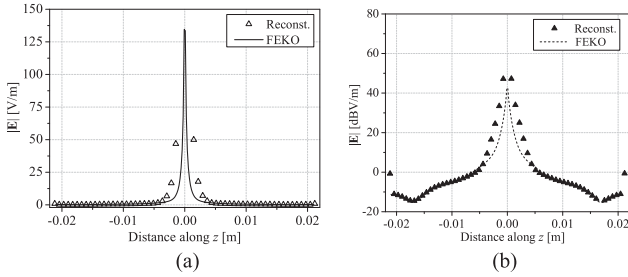


Fig. 5. $|\mathbf{E}|$ distribution along the z -axis at $x = y = 0$ for a cuboid phantom. (a) Linear scale. (b) Corresponding logarithmic scale.

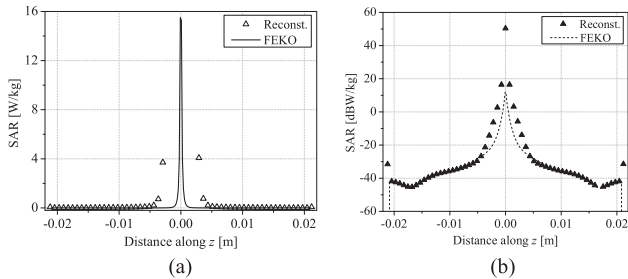


Fig. 6. Resultant SARs along the z -axis at $x = y = 0$ for a cuboid phantom. (a) Linear scale. (b) Corresponding logarithmic scale.

wave characteristics propagating across the phantom. For SAR, the logarithmic scale was calculated following the assumption of $\text{SAR}_{\text{dBW/kg}} = 10 \log(\text{SAR}_{\text{W/kg}})$. All figures are produced in absolute values. Remarkable accuracy can be seen from the boundary of the phantom to the entire interval except for near the antenna. The relative error was estimated at less than 4% for both $|\mathbf{E}|$ and SAR for distances of farther than ± 5 mm from the antenna center, while for points $-5 \text{ mm} < z < -0.7 \text{ mm}$ and $0.7 \text{ mm} < z < 5 \text{ mm}$, the error was 36.5%. The limitation to calculate smaller distances than these is noted, as the absolute error was immense in antenna vicinity.

It should be noted here that the meshing selection on the simulator is particularly sensitive and affects both magnitude and phase of the generated field data and consequently the reconstructed surface currents on S_P . Fig. 7(a) shows the ray representation of the radiated field from the AUT [21], [22]. In the region over the AUT where the incident angle (θ_i) to the interface (I) is smaller than the critical angle of total reflection (θ_c), the field is approximately represented by the geometrical optics (GO) ray that satisfies Snell's law. The field with incident

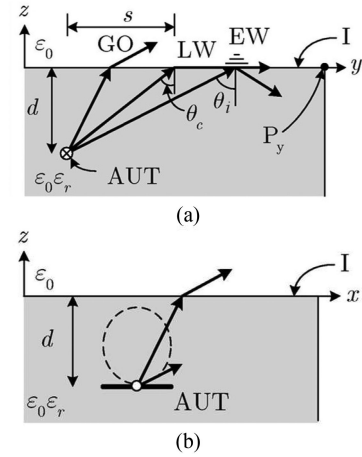


Fig. 7. Ray representation for radiated field from AUT. (a) yz -plane. (b) xz -plane.

angle $\theta_i > \theta_c$ is divided into two components. One of which is the lateral wave (LW) that coincides with θ_c at the interface and propagates along the surface. In this instance, the LW is diffracted at the edge of the phantom P_y . The other wave is the one propagating toward the interface just below the observation point and approaches as an evanescent wave that decays exponentially.

Since θ_c is given by $\theta_c = \sin^{-1}(\frac{1}{n})$, where $n = \sqrt{\epsilon_r}$ is the refractive index of the phantom, the aperture size $s = d \tan \theta_c$ for the GO ray becomes small when ϵ_r indicates a large value, such as the human body. Hence, the field over the interface where the reconstruction takes place theoretically is changing very rapidly. The field in the xz -plane behaves similarly, but the LW component here is fundamentally small due to the angular characteristic of the radiated field, as expressed by the dashed line, as shown in Fig. 7(b). It is found from some numerical examples that an average mesh of $0.1\lambda_{ph}$ or smaller is needed for the stable computation of cuboidal phantom, as discussed in this article, where $\lambda_{ph} = \lambda/n$ is the wavelength in the phantom. If the curvature of the phantom is small, the above criterion for the mesh size may be applied.

However, in the case of a large curvature object, such as a sphere, the sensitivity of meshing selection on the simulator increases because a curved surface might have caused the ray of fields from each individual mesh triangle to become severely angled compared with flat surfaces, such as a cuboid. This hypothesis was tested using a horizontal dipole radiating inside a lossless, dielectric sphere of radius $r_S = 3 \text{ cm}$ with permittivity $\epsilon_r = 1.5$ of which is arbitrarily selected to test a low-permittivity object. The reconstruction results are arranged in the same manner, as shown in Figs. 5 and 8. The other parameters, including mesh size, are retained as that of Section III-A. In Fig. 8(b), the $|\mathbf{E}|$ distribution in the range from $\pm 0.02 \text{ m}$ to $\pm 0.01 \text{ m}$ has a distinguishable error compared with the cuboid, even though the object is of much lower permittivity and is essentially a lossless dielectric. Moreover, it is also identified that conductivity is not a casual element contributing to this phenomenon.

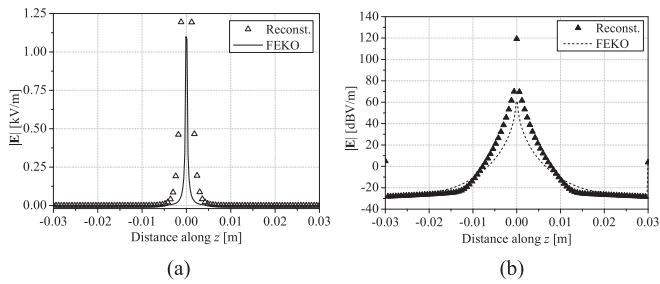


Fig. 8. $|E|$ distribution along the z -axis at $x = y = 0$ for a sphere. (a) Linear scale. (b) Corresponding logarithmic scale.

TABLE I
RECIPE OF PHANTOM

Ingredients	Quantity [g]	Role
Deionized water	420	Main component
Agar	20	Maintain shape
Polyethylene powder (PEP)	47	Controls ϵ_r and σ
Sodium chloride	2.1	Controls ϵ_r and σ
TX-151	6.25	Thickener
Sodium dehydroacetate monohydrate	0.25	Preservative

While an extremely fine mesh is used for precisely modeling such objects and avoid such occurrence, a larger size is used for reconstructing the surface currents in most cases because the inversion process imposes heavy computational loads, including the computer memory.

IV. EXPERIMENTAL VALIDATION

In this section, we performed experiments in order to confirm the validity and effectiveness of the proposed method. The experiment was done using a cuboid phantom of a similar dimension as the one presented in Section III. The phantom fabrication will be briefly explained before discussing the experimental setup inside an anechoic chamber.

A. Phantom Fabrication and Measurement

An agar-based cuboid phantom is prepared by referring to the articles presented in [23] and [24] with some adjustment to the material ratio by trial and error. The manufacturing process is simple, and it can be made with nonindustrial grade equipment. The composition of ingredients is listed in Table I and the steps to fabricate it are as follows.

Steps to fabricate the phantom are as follows.

- 1) Mix the deionized water, agar, sodium chloride, and sodium dehydroacetate monohydrate until dissolved.
- 2) Heat the mixture until bubbles start to form. The mixture will thicken and becomes slightly translucent.
- 3) Transfer the heated mixture into a mixer.
- 4) Add the TX-151 and PEP in parts, until finished.
- 5) Pour the final mixture into the desired mold in a controlled manner to minimize air bubbles.
- 6) Let cool it down completely in room temperature before storage.

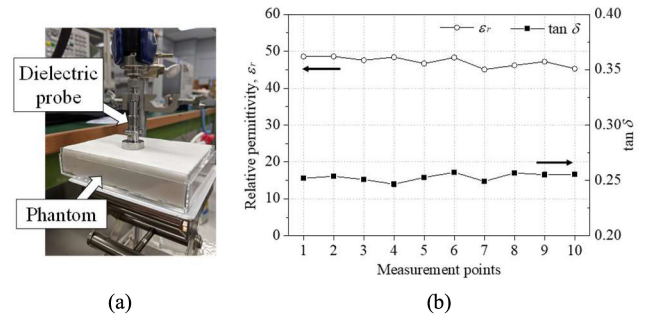


Fig. 9. Measurement of dielectric constant at 2.5 GHz. (a) Dielectric probe and cuboid phantom. (b) Measured data of ϵ_r and $\tan \delta$.

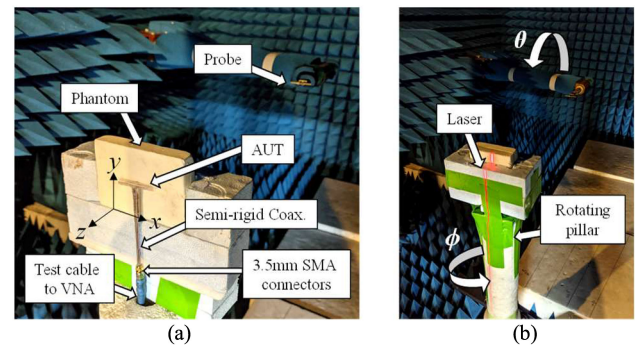


Fig. 10. Experimental setup in an anechoic chamber. (a) Phantom with AUT before being fully enclosed. (b) Complete setup. A laser module is used for more precise alignment.

Step 4) plays a crucial role to achieve the desired value of the dielectric constant because PEP is the active ingredient that determines the dielectric constant of the phantom. This step must be done swiftly before the agar component starts to coagulate. The delay in mixing may cause the powder not to be mixed thoroughly before the phantom solidifies, causing the permittivity and/or conductivity to divert than that of the target value, due to changing of ingredient's ratio.

The dielectric properties are then measured using Agilent Technologies (Keysight) 85 070 dielectric probe kit connected to E8364B PNA series network analyzer at ten different spatial points, as shown in Fig. 9. The constant readings ensure the stability of phantom for the measurement use. For input of computer program, the average value is calculated and is given as follows: $\epsilon_r = 48.7$ and $\tan \delta = 0.25$, the latter corresponding to $\sigma = 1.66$ (S/m). The measured dielectric constant is close to a human skin tissue [25]. For our study, the dimensions of geometries and dielectric parameters in numerical simulations are adjusted based on the finished product of a measured phantom for ease of comparison.

B. Experimental Setup

The experiment was performed using the phantom manufactured in Section V-A. Fig. 10 shows the photograph of the experimental setup. The transmitter (Tx) or AUT is a dipole of length $\ell_d = 30$ mm ($\sim 0.25\lambda$ in vacuum or $1.7\lambda_{ph}$ in phantom), mounted on a semirigid coaxial cable by a 3.5 mm

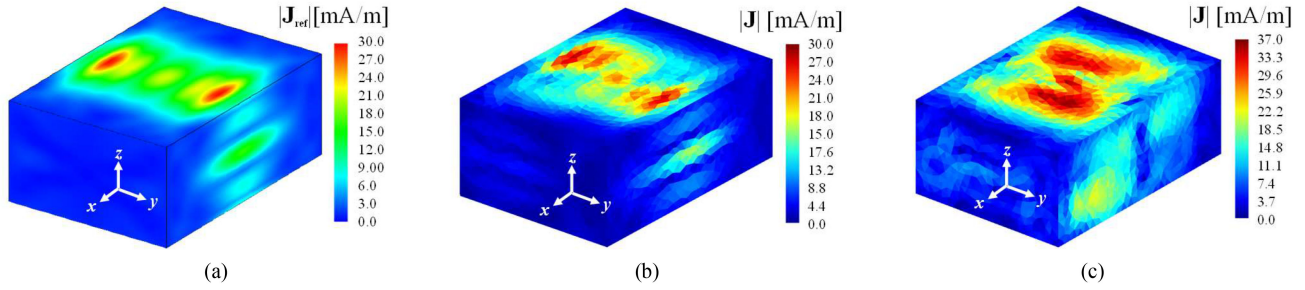


Fig. 11. Reconstructed electric current distribution on S_P . (a) Generated directly from FEKO. (b) Using simulator's probe data. (c) Using measured probe data.

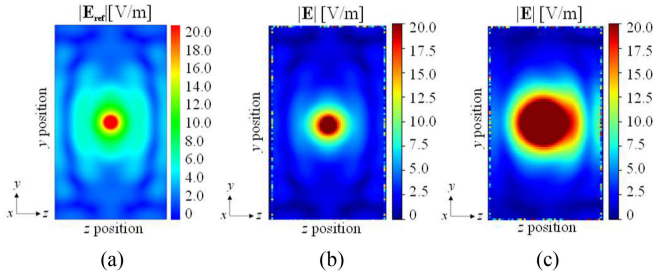


Fig. 12. Reconstructed internal electric field. (a) Generated directly from FEKO. (b) Using simulator's probe data. (c) Using measured probe data.

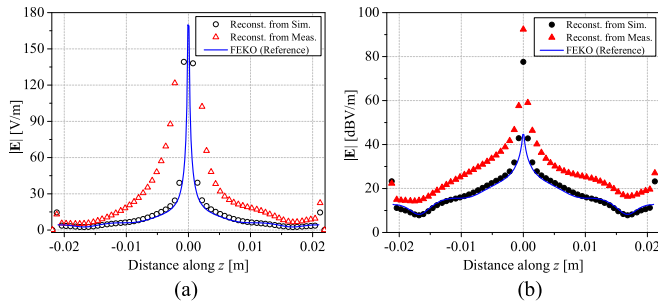


Fig. 13. $|E|$ distribution along the z -axis at $x = y = 0$ for experimental values. (a) Linear scale. (b) Corresponding logarithmic scale.

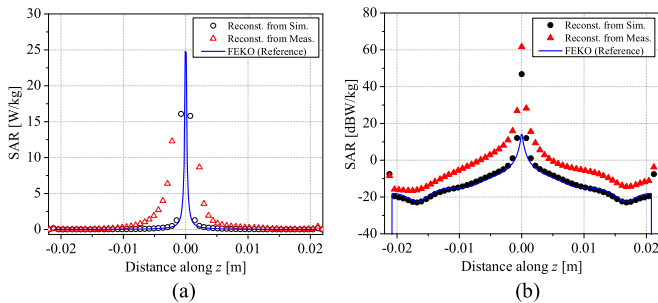


Fig. 14. Resultant SARs along the z -axis at $x = y = 0$ for experimental values. (a) Linear scale. (b) Corresponding logarithmic scale.

SubMiniature version A (SMA) connector. The radiating element and the coaxial cable are covered with a thin layer of common polyethylene plastic film of minimal thickness, just sufficient to avoid direct contact with the dielectric surface. The dipole is placed in one part of the phantom before enclosing the other half. This configuration is then securely held using

polystyrene foam [4]. The usage of polyethylene plastic film and the polystyrene foam as a holder and/or spacer in mobile antenna measurement is compliant with the standardization set by the International Electrotechnical Commission, which states that the fixture to hold AUT in test position must be a low permittivity and low loss material [26], such as used in this setup.

The phantom embedded with AUT was placed on the horizontally rotating azimuth (ϕ) table. The receiving (Rx) probe that we used is a 48 mm horizontal Schwarzbeck UHA 9125D half-wavelength dipole with electromagnetic interference balun [27] and was fixed to an arm rotated about the vertical axis (θ). The forward voltage was measured using Agilent Technologies E5071C vector network analyzer (VNA), with the probe at 0.6 m (5λ) distance from the center of AUT in the interval of the elevation angle being $0 \leq \theta \leq \pi/2$. The angular sampling interval was set to $\Delta\theta = \Delta\phi = 5^\circ$. Although a full sphere probe scanning is better for more accurate and symmetrical results, a hemisphere scanning was performed due to the limitation of hardware of the experimental setup, and it also saves calculation time [28].

It would be ideal if the numerical solution of Section III is experimentally performed using the same antenna. However, the 4.3 mm short dipole was too small to fabricate with precision by a thin wire. Following that, the simulation and experimental procedure were performed again using a longer antenna. From a theoretical point of view, the current distribution profile of a short dipole antenna is a simple, almost triangular pattern, while a longer dipole here has a more complicated sinusoidal pattern with more than one maximum peak value [29]. Therefore, the applicability of the proposed method would be assessed by a more complicated current distribution. Besides that, it is also arduous for a typical anechoic chamber setup to efficiently collect the low-level signal radiated from the compact AUT inside of phantom because E -field wave traversing through a lossy material decreases exponentially due to the loss created by effective conduction currents [30]. For these two reasons, a slightly longer length AUT compared with that of Section III was used in the experiment in order to assess the applicability of ECM-SR when a more complicated current distribution is involved and to expect an enlargement of radiation power.

C. Reconstruction Results

Let us compare the reconstructed results. This section considers three results; one of which is the results directly generated

by FEKO, which is used as a reference, the second and third are reconstructions using probe data from FEKO and measured, respectively. All parameters used in these calculations were described in Section V-A and B, except for the solver's error tolerance increased to 10^{-3} to compensate for the measurement errors and to prevent the equation system from falling into the local solution.

Fig. 11 and Fig. 12 are the surface current and electric field distribution, respectively. Fig. 11(b) exhibits evident asymmetrical distribution property compared with reference that is Fig. 11(a), even though the probe data are originated from an ideal simulation environment. This is contrary to reconstruction results, as previously presented in Fig. 3, showing that utilizing a longer AUT size of almost seven times longer considerably affects the reconstruction results of the current and field distributions. Thus, for a steady increase in accuracy, the AUT should be gradually minimized with respect to wavelength in the dielectric material. Meanwhile, the reconstruction in Fig. 11(c) is roughly acceptable when compared with both Fig. 11(a) and (b), considering that the experimental setup data were used for the calculations. Nevertheless, distinct characteristics of a horizontally polarized dipole radiation can be seen for both reconstructed results; high current density concentrated on the center area, lower on the left and right sides. From the current distribution data, we reconstructed the internal electric field distribution, as presented in Figs. 12 and 13. The results are satisfactory and were also confirmed from Fig. 14 where the concurrent SAR calculated from it are shown along the z -axis at $x = y = 0$.

The most predominant challenge is mechanically aligning the probe during the experimental procedure. Although we have used a laser in the initial setup to ensure that the Tx and Rx probes are precisely aligned, as described in Fig. 10, the rotating position for each angular point \mathbf{R} could not be monitored directly during the data collection. This may have caused the magnitude and phase of the collected $\mathbf{E}(\mathbf{R})$ to deviate from that of the expected value and ultimately affecting the reconstruction results. Therefore, utilizing a high-precision arm to overcome mechanical inaccuracies in the field sampling results is one of the possible solutions. However, it is considered a hardware-related issue and may be more costly to address; hence, the correction at the computational level might be more feasible.

V. CONCLUSION

In this article, we have proposed an SR method to obtain the internal electric field of the phantom with an embedded antenna. This method is effectively applicable to the noninvasive SAR dosimetry of small biomedical telemetry devices if the dielectric constants are known in advance. The reconstruction is based on PMCHWT formulation by discretizing all the integral equations that relate the scattered radiation fields and relating it to the EM currents of the antenna and on the surface of the phantom using a current equivalence theorem. Probe correction is also applied to compensate the influence of inverse operators and probe's receiving characteristic on the surface of measurement. This method was verified numerically and experimentally using the dipole antenna inside of the lossy cuboid phantom. The results were accurate for a very compact AUT in the evaluation

of relative error but suffers as the length of the radiating element elongates in which the solver's error tolerance needs to be increased for stable computation. The reconstruction is also challenging to be applied in a heterogenous structure and in calculating points very close to the center of the antenna due to the boundary integral formulations.

Besides what has been previously suggested, another potential extension to this work is the localization of AUT. In this work, the reconstruction surface of AUT is known. But in a real wireless telemetry device, an additional degree of freedom, which is the location and depth inside the body, is not static. Therefore, the reconstruction surface will also be constantly changing. The idea is using ECM-SR to predict antenna location from the maximum magnitude of the reconstructed internal electric field. We look forward to see interesting outcomes in the future.

ACKNOWLEDGMENT

The authors would like to thank Dr. K. Sasaki of the Applied Electromagnetic Research Institute, National Institute of Information and Communications (NICT), Koganei, Tokyo, for his guidance and advice regarding phantom measurement using NICT's facility.

REFERENCES

- [1] K. S. Nikita, *Handbook of Biomedical Telemetry*. Hoboken, NJ, USA: Wiley, 2014.
- [2] Medtronic, Dublin, Ireland. Accessed: Sep. 29, 2020. [Online]. Available: <https://www.medtronic.com/covidien/en-us/products/capsule-endoscopy.html>
- [3] Int. Commission Non-Ionizing Radiat. Protection, "ICNIRP guidelines for limiting exposure to time-varying electric, magnetic and electromagnetic fields (up to 300 GHz)," *Health Phys.*, vol. 74, no. 4, pp. 494–522, Apr. 1998.
- [4] H. Arai, *Measurement of Mobile Antenna Systems*. Norwood, MA, USA: Artech House, 2013, pp. 119–120.
- [5] B. McDermott *et al.*, "Anatomically and dielectrically realistic microwave head phantom with circulation and reconfigurable lesions," *Prog. Electromagn. Res. B*, vol. 78, pp. 47–60, Jan. 2017.
- [6] O. Bottauscio, M. Chiampi, and L. Zilberti, "A boundary element approach to relate surface fields with the specific absorption rate (SAR) induced in 3-D human phantoms," *Eng. Anal. Boundary Elements*, vol. 35, no. 4, pp. 657–666, Apr. 2011.
- [7] O. Bottauscio, M. Chiampi, and L. Zilberti, "Boundary element solution of electromagnetic and bioheat equations for the simulation of SAR and temperature increase in biological tissues," *IEEE Trans. Magn.*, vol. 48, no. 2, pp. 691–694, Feb. 2012.
- [8] J. L. A. Quijano and G. Vecchi, "Field and source equivalence in source reconstruction on 3D surfaces," *Prog. Electromagn. Res.*, vol. 103, pp. 67–100, Aug. 2010.
- [9] R. Mitharwal and F. P. Andriulli, "A regularised boundary element formulation for contactless SAR evaluations within homogeneous and inhomogeneous head phantoms," *Comptes Rendus Physique*, vol. 16, no. 9, pp. 776–788, Nov. 2015.
- [10] S. Omi, T. Uno, T. Arima, and J. Wiart, "Reconstruction of internal field of dielectric objects for noninvasive SAR measurement using boundary integral equation," *IEEE Trans. Electromagn. Compat.*, vol. 61, no. 1, pp. 48–56, Feb. 2019.
- [11] M. Phaneuf and P. Mojabi, "Electromagnetic inversion for noninvasive specific absorption rate characterization," *IEEE J. Electromagn. RF Microw. Med. Biol.*, vol. 4, no. 4, pp. 254–259, Dec. 2020.
- [12] K. Cools, F. P. Andriulli, and E. Michielssen, "A Calderón multiplicative preconditioner for the PMCHWT integral equation," *IEEE Trans. Antennas Propag.*, vol. 59, no. 12, pp. 4579–4587, Dec. 2011.
- [13] W. C. Gibson, *The Method of Moments in Electromagnetics*. Boca Raton, FL, USA: CRC Press, 2008.
- [14] S. Rao, D. Wilton, and A. Glisson, "Electromagnetic scattering by surfaces of arbitrary shape," *IEEE Trans. Antennas Propag.*, vol. 30, no. 3, pp. 409–418, May 1982.

- [15] T. F. Eibert, E. K. Ismatullah, and C. H. Schmidt, "Inverse equivalent surface current method with hierarchical higher order basis functions, full probe correction and multilevel fast multipole acceleration," *Prog. Electromagn. Res.*, vol. 106, pp. 377–394, Jul. 2010.
- [16] Y. J. Yoon and B. Kim, "A new formula for effective dielectric constant in multi-dielectric layer microstrip structure," in *Proc. IEEE 9th Topical Meeting Elect. Perform. Electron. Packag.*, 2000, pp. 163–167.
- [17] D. Rano, M. A. Chaudhary, and M. S. Hashmi, "A new model to determine effective permittivity and resonant frequency of patch antenna covered with multiple dielectric layers," *IEEE Access*, vol. 8, pp. 34418–34430, 2020.
- [18] "Federal communications commission office of engineering and technology, policy and rules division," Federal Communications Commission, Washington, DC, USA, Feb. 1, 2021. Accessed: Mar. 15, 2021. [Online]. Available: <https://transition.fcc.gov/oet/spectrum/table/fcctable.pdf>
- [19] M. R. Basar, F. Malek, K. M. Juni, M. S. Idris, and M. I. M. Saleh, "Ingestible wireless capsule technology: A review of development and future indication," *Int. J. Antennas Propag.*, vol. 2012, Dec. 2012, Art. no. 807165.
- [20] C. Geuzaine and J.-F. Remacle, "Gmsh: A three-dimensional finite element mesh generator with built-in pre- and post-processing facilities," *Int. J. Numer. Methods Eng.*, vol. 79, no. 11, pp. 1309–1331, Sep. 2009.
- [21] Y. He, M. Maruyama, T. Uno, S. Adachi, and T. Mashiko, "Dipole antenna reception of transient electromagnetic fields refracted from a dipole antenna buried in a lossy half-space," *IEICE Trans. Electron.*, vol. E74, no. 9, pp. 2870–2876, Sep. 1991.
- [22] A. Ishimaru, *Electromagnetic Wave Propagation, Radiation, and Scattering: From Fundamentals to Applications*, 2nd ed. Hoboken, NJ, USA: Wiley, 2017.
- [23] K. Ito, K. Furuya, Y. Okano, and L. Hamada, "Development and characteristics of a biological tissue-equivalent phantom for microwaves," *Electron. Commun. Jpn.*, vol. 84, no. 4, pp. 67–77, Apr. 2001.
- [24] T. Onishi, and S. Uebayashi, "Biological tissue-equivalent phantoms usable in broadband frequency range," *NTT DoCoMo Tech. J.*, vol. 7, no. 4, pp. 61–65, 2006.
- [25] C. Gabriel and S. Gabriel, "Compilation of the dielectric properties of body tissues at RF and microwave frequencies," Physics Dept., King's College London, London, U.K., Tech. Rep. AL/OE-TR-1996-0037, 1996.
- [26] *Human Exposure to Radio Frequency Fields from Hand-Held and Body-Mounted Wireless Communication Devices—Human Models, Instrumentation, and Procedures—Part 2: Procedure to Determine the Specific Absorption Rate (SAR) for Wireless Communication Devices Used in Close Proximity to the Human Body (Frequency Range of 30 MHz to 6 GHz)*, IEC 62209-2, Int. Electrotech. Commission, Geneva, Switzerland, 2010.
- [27] "UHA 9125 D - Half wave dipole with EMI-balun," Schwarzbeck Mess - Elektronik OHG, Schönau, Germany, 2013–2020. Accessed: Dec. 12, 2020. [Online]. Available: <http://www.schwarzbeck.de/en/antennas/precision-dipoles>
- [28] J. E. Hansen, J. Hald, F. Jensen, F. H. Larsen, and J. R. Wait, *Spherical Near-Field Antenna Measurements*. London, U.K.: Inst. Eng. Technol., 2008.
- [29] W. L. Stutzman and G. A. Thiele, *Antenna Theory and Design*, 3rd ed. Hoboken, NJ, USA: Wiley, 2012, pp. 151–153.
- [30] C. Furse, D. A. Christensen, C. H. Durney, and J. Nagel, *Basic Introduction to Bioelectromagnetics*. Boca Raton, FL, USA: CRC Press, 2019, pp. 39–40.



Rasyidah Hanan Mohd Baharin (Student Member, IEEE) received the B.E. degree in computer network engineering from Universiti Malaysia Perlis, Kangar, Malaysia, and the M.E. degree in electronic system engineering from Universiti Teknologi Malaysia (UTM), Kuala Lumpur, Malaysia, in 2015 and 2017, respectively. She is currently working toward the Ph.D. degree electronic and information engineering with the Department of Electronics and Information Engineering, Tokyo University of Agriculture and Technology, Tokyo, Japan.

From 2017 to 2018, she was a Research Assistant with Communication Systems and Networks Laboratory, Malaysia-Japan International Institute of Technology, UTM. Her current research interests include inverse methods and antenna in biomedical applications.

Ms. Mohd Baharin was a recipient of the Student Paper Award in the 2020 International Symposium on Antennas and Propagation, Osaka, Japan.



Shuntaro Omi (Member, IEEE) received the B.E., M.E., and Ph.D. degrees in engineering from the Tokyo University of Agriculture and Technology, Tokyo, Japan, in 2014, 2016, and 2019, respectively.

From 2019 to 2020, he was a Postdoctoral Researcher with the National Institute of Advanced Industrial Science and Technology, Tsukuba, Japan. He is currently a Postdoctoral Researcher with the National Institute of Information and Communications Technology, Tokyo, Japan. His current research interest focuses on antenna measurement techniques.

Dr. Omi was a recipient of the Student Award and the Young Engineer Award from the IEEE Antennas and Propagation Society Japan Chapter.



Toru Uno (Senior Member, IEEE) received the B.E. degree in electrical engineering from the Tokyo University of Agriculture and Technology (TUAT), Tokyo, Japan, in 1980, and the M.S. and Ph.D. degrees in electrical engineering from Tohoku University, Sendai, Japan, in 1982 and 1985, respectively.

From 1985 to 1991, he was a Research Associate with the Department of Electrical Engineering, Tohoku University, and from 1991 to 1994, an Associate Professor. From 1998 to 1999, he was on leave from the TUAT. He was a Visiting Scholar with the Department of Electrical Engineering, Pennsylvania State University, State College, PA, USA.

He is currently a Professor with the Department of Electrical and Electronics Engineering, TUAT.

Dr. Uno was a recipient of the Young Scientist Award, the Distinguished Contributions Award, and the Paper Award from the IEICE in 1990, 2006, and 2007, respectively. He served as the Chair of the IEEE Antennas and Propagation Society Japan Chapter from 2005 to 2006 and an Associate Editor for the *IEEE Antennas and Wireless Propagation Letters* from 2008 to 2013. From 2011 to 2012, he was the Chair of the Technical Group on Antennas and Propagation, Institute of Electronics, Information and Communications Engineers (IEICE) and a General Chair of the 2016 International Symposium on Antennas and Propagation. He is currently a Fellow of the IEICE.



Takuji Arima (Member, IEEE) received the M.E. and D.E. degrees in engineering from the Tokyo University of Agriculture and Technology, Tokyo, Japan, in 1999 and 2002, respectively.

He is currently an Associate Professor with the Department of Electrical and Electronics Engineering, Tokyo University of Agriculture and Technology, and a Part-Time Researcher with the National Institute of Information and Communications Technology, Tokyo, Japan. His research interests include computational electromagnetics and metamaterials.

Dr. Arima was a recipient of the Young Scientist Award from the IEEE Antennas and Propagation Society Japan Chapter.